

Discovery of 19 strongly-lensed quasars, dual and projected quasars in DESI-LS

Zizhao He¹, Qihang Chen^{2,3}, Limeng Deng^{1,4}, Yiping Shu¹, Rui Li⁵, Nan Li⁶, Dongdong Shi⁷, and Guoliang Li¹

¹ Purple Mountain Observatory, Chinese Academy of Sciences, Nanjing, Jiangsu, 210023, China
e-mail: zzhe@pmo.ac.cn

² School of Physics and Astronomy, Beijing Normal University, Beijing, 100875, China

³ Institute for Frontier in Astronomy and Astrophysics, Beijing Normal University, Beijing, 102206, China

⁴ School of Astronomy and Space Sciences, University of Science and Technology of China, Hefei 230026, China

⁵ Institute for Astrophysics, School of Physics, Zhengzhou University, Zhengzhou, 450001, China

⁶ Key lab of Space Astronomy and Technology, National Astronomical Observatories, 20A Datun Road, Chaoyang District, Beijing 100012, China;

⁷ Centre for Fundamental Physics, School of Mechanics and Optoelectric Physics, Anhui University of Science and Technology, Huainan, Anhui 232001, China

Received September 15, 1996; accepted March 16, 1997

ABSTRACT

We report the follow-up spectroscopic confirmation of two lensed quasars, six dual quasars, and eleven projected quasars that were previously identified as lensed-quasar candidates in He et al. (2023). The spectroscopic data were obtained from two different sources: the P200/DBSP in California and publicly available datasets, including SDSS and DESI-EDR. The two lensed quasars (both pairs) have the following properties: $\theta_E = 1''.208$, $z_s = 3.105$; $\theta_E = 0''.749$, $z_s = 2.395$. The six dual quasars have redshifts ranging from 0.58 to 3.28 and projected separations ranging from 15.44 to 22.54 kpc, with a mean separation of 17.95 kpc. The eleven projected quasars have projected separations ranging from 10.96 to 39.07 kpc, with a mean separation of 22.64 kpc. Additionally, there are three likely lensed quasars that cannot be definitively confirmed, contributed by two reasons. Firstly, their image separations ($0''.83$, $0''.98$, and $0''.93$) are small compared to the seeing conditions during our observations (around $1''.2$). Secondly, no high SNR lensing galaxy can be detected in the Legacy Survey Imaging. Better spectroscopy and (or) imaging are needed to confirm their lensing nature.

Key words. gravitational lensing: strong – (galaxies:) quasars: general

1. Introduction

When two quasars with a small separation are observed, there are often three different physical scenarios. The most common scenario is projected quasars, where quasars coincidentally appear very close to each other along the line of sight, but are actually at vastly different redshifts. A rarer scenario is dual quasars, which are at similar redshift and physically interacting. The rarest scenario is lensed quasars, where the light from a single quasar is bent, resulting in two images of the same quasar. In that case, an intervening lensing galaxy is usually expected.

The three categories mentioned above each play different roles in the investigation of the universe. Gravitationally lensed quasars not only enable investigations traditionally addressed by galaxy-galaxy lenses, such as constraining the equation of state of dark energy and investigating galaxy evolution (Oguri et al. 2014; Suyu et al. 2014; Shu et al. 2015; Sonnenfeld & Cautun 2021; Filipp et al. 2023), but also provide a unique avenue for measuring the Hubble constant (Shajib et al. 2018; Liao et al. 2019; Wong et al. 2020; Li et al. 2021). Moreover, they offer information on the structures of active galactic nuclei (AGNs) (Anguita et al. 2008; Sluse et al. 2011; Motta et al. 2012; Guerras et al. 2013; Braibant et al. 2014; Fian et al. 2021; Hutsemékers & Sluse 2021). Dual quasars, which refer to quasar pairs separated by 1 pc to 100 kpc (De Rosa et al. 2019), have considerable significance in elucidating the growth and evolution

of binary supermassive black holes (BSMBHs, Roedig et al. 2014; Romero et al. 2016) and illuminating the processes of galactic-scale merging (Boylan-Kolchin et al. 2008; Martin et al. 2018). Projected quasars can be used to study the circumgalactic medium (CGM, Cai et al. 2019) properties of quasar host galaxies (Findlay et al. 2018; Chen et al. 2023).

The discovery of those objects involves two key stages: candidate selection followed by spectroscopy confirmation. The first often rely on imaging surveys such as Dark Energy Spectroscopic Instrument Legacy Imaging Surveys (DESI-LS, Dey et al. 2019), Kilo Degree Survey (KiDS, de Jong et al. 2019), Dark Energy Survey (DES, The Dark Energy Survey Collaboration 2005), Panoramic Survey Telescope and Rapid Response System (Pan-STARRS, Chambers et al. 2016), or astrometric satellites such as Gaia (Gaia Collaboration et al. 2018). The second relies on spectroscopic surveys, such as the Sloan Digital Sky Survey (SDSS, Blanton et al. 2017) and the Dark Energy Spectroscopic Instrument (DESI, DESI Collaboration et al. 2016), and targeted follow-up observations (e.g., Lemon et al. 2022; Dux et al. 2023, 2024).

Based on random forest selection and DESI-LS data, 620 new candidate lensed quasars have been collected in He & Li (2022); He et al. (2023). In this study, we selected ten high-priority observable candidates from He et al. (2023) and obtained their spectra using the DBSP/P200 at Palomar Obser-

vatory. Most of these targets exhibit separations smaller than $2.4''$. Prior to our observations, we checked these targets in recently available spectral datasets, including SDSS DR16 and DESI EDR, to verify whether they had been spectroscopically observed in recent surveys. For confirmed lensed quasars, we performed light and lens modelling to reveal their properties. For confirmed dual quasars, we calculated velocity differences, determined projected separations, and discussed CGM features.

The structure of this paper is as follows. Section 2 details the observational aspects, including a review of the target selection process, spectral data reduction procedures, and specifics of spectroscopic follow-up. Sections 3 and 4 present the confirmation results of P200/DBSP observations and publicly available datasets, respectively. Finally, Section 5 provides a comprehensive discussion and summary of our findings. In this paper, a fiducial cosmological model with $\Omega_m = 0.26$, $\Omega_{DE} = 0.74$, $h = 0.72$, $w_0 = -1$, and $w_a = 0$ is assumed. Unless otherwise stated, all magnitudes quoted in this paper are in the AB system.

2. Observations

In Section 2.1, we briefly review the target selection process, with further details available in He & Li (2022); He et al. (2023). Section 2.2 introduces the spectroscopic equipment setups and observing conditions. Finally, Section 2.3 provides a brief overview of the spectral data reduction process.

2.1. Target selection

The first step in our approach involves employing a Random Forest (RF) classifier to identify quasar candidates from the DESI Legacy Surveys (DESI-LS) photometry catalogue. Our training set comprises 651,073 positive and 1,227,172 negative samples, incorporating photometric data from both DESI-LS and the Wide-field Infrared Survey Explorer (WISE). The labels for these samples were derived from the Sloan Digital Sky Survey (SDSS) and the Set of Identifications, Measurements, and Bibliography for Astronomical Data (SIMBAD).

We applied the trained RF model to point-like sources in DESI-LS Data Release 9. The performance of the classifier, evaluated using a test set, demonstrated a recall of $\sim 99\%$ at a purity of $\sim 30\%$. Through this process, we successfully identified approximately 24 million quasar candidates from a pool of ~ 0.42 billion point-like sources. In the second phase, we designed a quasar group finder algorithm based on spatial coordinates to identify quasars in close proximity to each other. This algorithm initially generated $\sim 560,000$ quasar groups from the ~ 24 million quasar candidates. We then refined these groups by analysing the similarity of colours among group members and their likelihood of being quasars. This refinement process reduced the number of quasar groups from $\sim 560,000$ to $\sim 140,000$.

The final stage involved visual inspection to select candidate strongly lensed quasars based on the spatial configuration of group members. During this process, we classify candidates into categories A, B, and C, with grade A representing the most promising candidates. This examination yielded 620 new lensed quasar candidates, consisting of 101 grade-A, 214 grade-B, and 305 grade-C candidates. Following the name used in He et al. (2023), we refer to the catalogue as H22.

2.2. Spectroscopic follow-up

The selection of targets followed a two-step process. The criteria of the first step were:

- Magnitudes of quasars are brighter than 21.5 in r -band;
- No prior spectroscopic observations reported;
- Classified as grade A or B in H22;
- Observable in Palomar observatory on October 15-16, 2023.

Subsequently, two additional conditions were considered, and it is sufficient for one of them to be met:

- A extend component can be identified between two point-like sources in the residuals of Legacy Survey Imaging;
- Also flagged as candidates in Dawes et al. (2023).

After applying these criteria, 21 targets were selected, of which 10 were observed due to weather constraints.

Long-slit spectroscopic follow-up was carried out for those ten candidates using the Double Spectrograph (DBSP) equipped on the P200 on the nights of 15-16 Oct. 2023 (P.I. Zizhao He). Their magnitudes and separations can be found in Table 1.

The brightest magnitude is $r = 18.45$ and the faintest is $r = 21.14$, with a median value of $r = 19.60$. The largest separation is $4''.65$ while the minimum is $0''.83$, with a median value of $1''.78$. The composite image of the grz bands can be found in Figure 1. The standard dichroic D-55 was used to split light into blue and red ends. The 300 lines/mm grating blazed at 3990 \AA was chosen for blue arms, while the 316 lines/mm grating blazed at 7150 \AA for red arms. This provides a dispersion of 2.108 \AA/pixel and 1.535 \AA/pixel for the blue and red arms (Oke & Gunn 1982).

Seeing conditions generally ranged between $0.9''$ and $1.5''$, and a $1.5''$ wide slit was utilized. For each exposure, the slit was aligned with two point sources, ensuring the sources were as close to the centre of the slit as possible. This approach ensured simultaneous and efficient acquisition of spectra for both sources.

Table 1 presents the key observational characteristics of the targets, including coordinates, exposure times, image separations, LS-DR10 r -band magnitudes, and the determined redshifts. In addition, the table provides the results of the spectroscopic identifications.

2.3. Spectral data reduction

The raw spectra were reduced using a PYTHON¹ code developed by us. The code utilizes several well-known Python modules, including Astropy (Astropy Collaboration et al. 2022), NumPy (Harris et al. 2020), and Pandas (Wes McKinney 2010). We implemented a standard data reduction procedure that includes bias subtraction, flat-fielding, cosmic ray rejection (Astroscrappy, McCully et al. 2018), 1D spectrum extraction, and wavelength and flux calibrations.

Wavelength calibration at the blue and red ends was performed using FeAr and HeNeAr blended arc lamps, respectively. Flux calibration for the blue end was carried out with standard stars Feige 15 and Feige 34, while the red end was calibrated using Feige 34. Furthermore, all reduced spectra, along with those from SDSS DR16 and DESI EDR, were smoothed using Gaussian filtering to reduce noise and enhance spectral features.

¹ <https://www.python.org/>

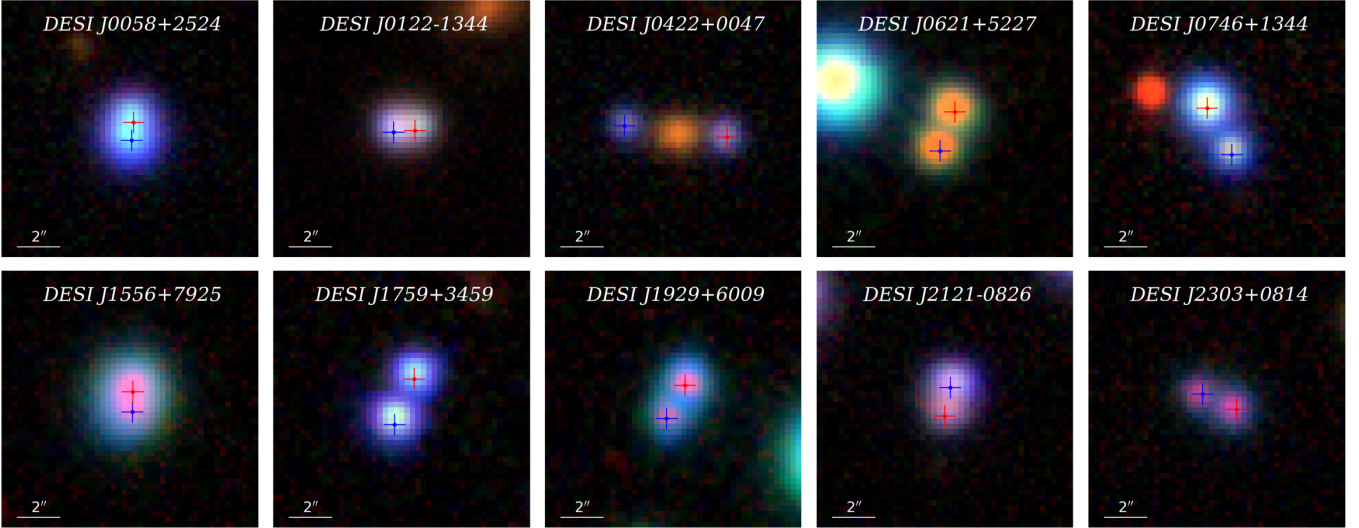


Fig. 1. DESI-LS colour images of the 10 targets observed by DBSP/P200 during Oct 15-16, 2023. The cutout size of each image is $12'' \times 12''$ and north is up while east is left. These cutout images are obtained from Legacy Survey Imaging DR10 in grz bands and re-plotted in this work using HumVI (Marshall et al. 2016).

Table 1. Observing table of 10 objects. ‘H22-ID’ is the ID of the system in He et al. (2023).

Name	H22-ID	RA(°)	Dec(°)	Exp. Time (s)	Separation (″)	r_{mag}	Quasar Redshift	Outcome
DESI J0058+2524	2459355	14.539675	+25.409982	1600	0.83	18.94, 19.71	2.580	likely lensed quasars
DESI J0122-1344	10930010	20.656958	-13.739587	2000	0.98	19.87, 20.26	1.420	likely lensed quasars
DESI J0422+0047	2893541	65.715309	+0.797050	4800	4.65	19.01, 19.23	1.982, 2.100	projected quasar + galaxy
DESI J0621+5227	1028529	95.478330	+52.461052	1200	1.92	19.41, 19.82	-	star + star
DESI J0746+1344	10721197	116.648160	+13.740173	1800	2.44	18.45, 20.04	3.105, 3.105	lens
DESI J1556+7925	1006023	239.157775	+79.427087	1500	0.93	18.75, 19.36	1.570	likely lensed quasars
DESI J1759+3459	2197502	269.825027	+34.991220	1800	2.30	19.56, 19.26	1.970, 1.982	dual quasar
DESI J1929+6009	10119139	292.255442	+60.156748	2100	1.74	19.50, 20.24	3.277, 3.277	dual quasar
DESI J2121-0826	10912799	320.384762	-8.436015	2400	1.34	19.63, 20.55	2.395	lens
DESI J2303+0814	2587254	345.939046	+8.248696	2100	1.82	20.71, 21.14	0.984, 0.928	projected quasar

Table 2. Light modelling results of lensing galaxies in two confirmed lensed quasars. The meaning of the n_s , r_s , q_s , ϕ_s can be found at Appendix A. m_s is the modelled apparent magnitudes in different bands. The $+x$ -axes is the $\phi_s = 0$, while the counterclockwise direction is considered the positive direction.

name	band	n_s	r_s	q_s	ϕ_s	m_s
J0746+1344	g			-		>23.0
	r			-		>23.0
	z	5.5 ± 1.3	0.9 ± 0.2	0.5 ± 0.1	27.0 ± 11.0	20.9 ± 0.3
J2121-0826	g	5.9 ± 0.2	0.4 ± 0.1	0.7 ± 0.1	-20.9 ± 5.4	21.3 ± 0.5
	r	3.2 ± 0.2	0.3 ± 0.1	0.6 ± 0.1	-26.0 ± 2.4	20.4 ± 0.2
	z	5.0 ± 0.7	0.1 ± 0.0	0.7 ± 0.1	-21.1 ± 2.2	19.8 ± 0.1

3. P200-DBSP Confirmation results

The observation results of ten targets using P200 in Palomar Observatory are presented here. Combining spectra and Legacy Survey Imaging, they were categorised into different classes, including lensed quasars (Section 3.1), likely lensed quasars (Section 3.2), dual quasars (Section 3.3), and projected quasars (Section 3.4). Spectroscopic analysis reveals that J0621+5227 is a star-star system composed of K-type stars. As this stellar system is out of the scope of our primary scientific objectives, we will not discuss it further in the subsequent analysis.

3.1. Confirmed lensed quasars

3.1.1. J0746+1344

Two point sources can be distinctly identified in the Legacy Survey Imaging, with r -band magnitudes 18.45 and 20.04 respectively, separated by $2.''44$. Spectroscopic analysis reveals two quasars at a redshift of $z = 3.105$, exhibiting similar continuum and broad emission line profiles. This resemblance suggests that this is a gravitationally lensed system. In the light modelling procedure, the grz -band images are fitted well by two point spreading functions (PSFs) that represent the lensed quasar images, along with one Sérsic profile that represents the lensing galaxy. See top line of Figure 3 for the image reconstruction results, and Appendix A for the details about light modelling.

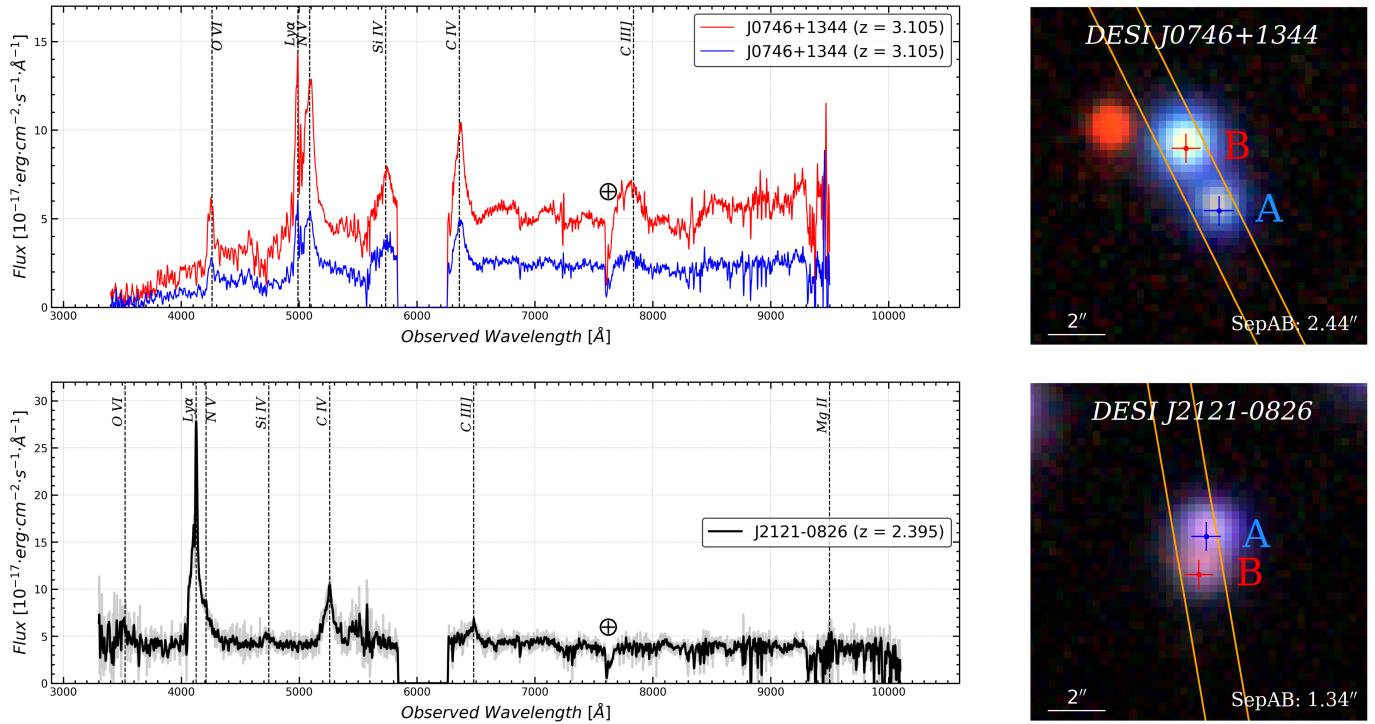


Fig. 2. The DBSP/P200 spectra and their corresponding cutout images of the two confirmed lensed quasars. The slit placement is labeled by the yellow lines.

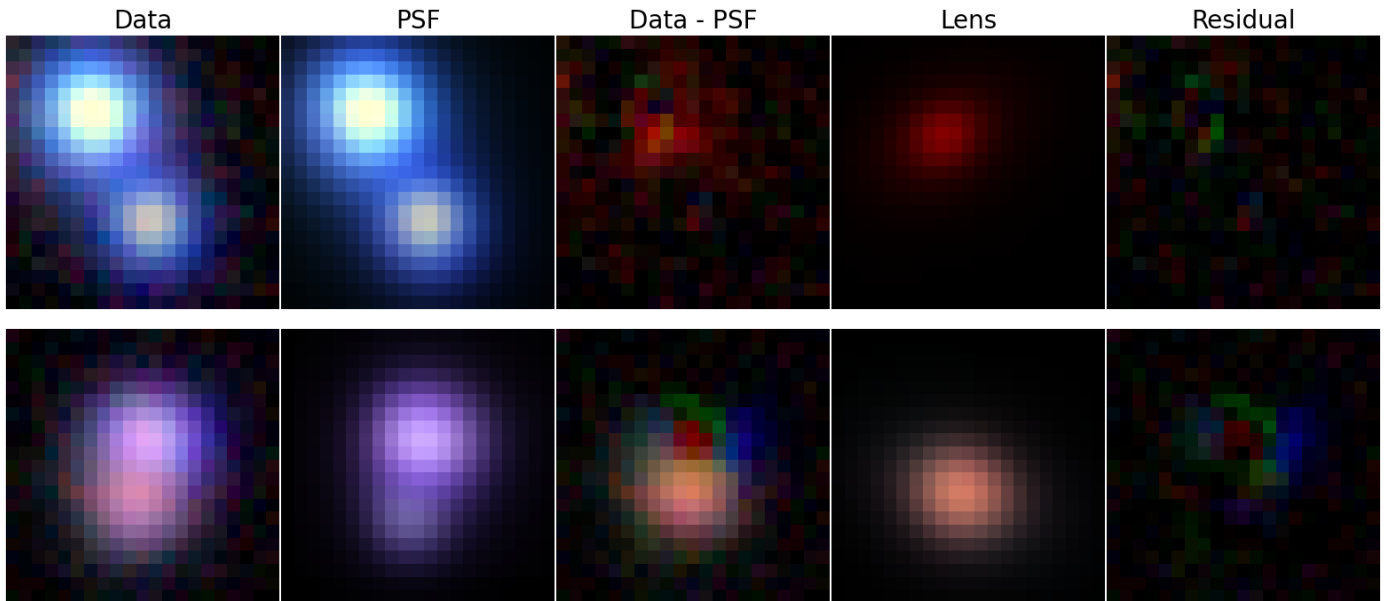


Fig. 3. The image decomposition results in *grz*-band for our confirmed lensed quasars. First: J0746+1344, Second: J2121-0826. First column (A): original data. Second (B): light model for two images. Third (C): A-B; Fourth (D): light model for best-fitted lensing galaxy assuming Sérsic profile. Fifth (E): A-B-D.

Based on the spectral similarities between the two quasar images, the detection of an extended component consistent with a lensing galaxy, and the successful fitting of a two-PSF plus Sérsic model fit, we classify this system as a gravitational lens. The light distribution of lensing galaxy is fitted by a single Sérsic profile, the results are summarised at Table 2. The results of multiple images are summarised at Table 3.

Lens modelling is further performed using Singular Isothermal Ellipsoid (SIE, Kormann et al. 1994) model. We inputted

the position of observed quasars, and assuming the SIE centre is same as light profile of lensing galaxy. The result of SIE is summarised at Table 4. Beside, the time-delay is estimated as a function of lens redshift, the result is given at Figure 5. The magnification (μ) of two images are also given in Table 3. The detailed methodologies used in mass modelling, and time-delay estimation, can be found at Appendix A.

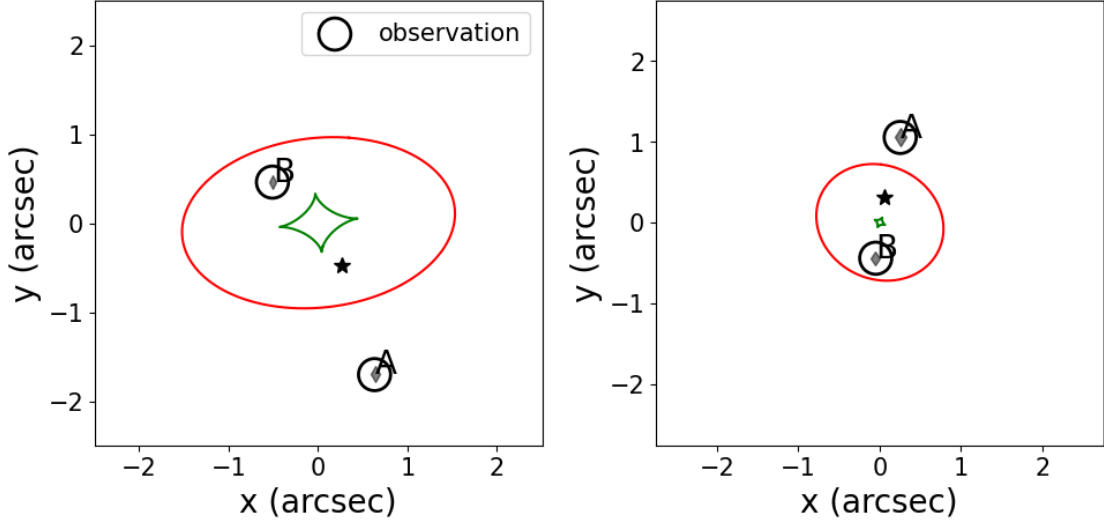


Fig. 4. The modelled caustic and critical curves, along with the positions of images for the two confirmed lenses shown in Figure 2, are compared with the observed positions of multiple images. The plots are centred around the lens light centre, which is determined through light modelling and provided in Table 4.

Table 3. The results of light modelling for multiple images of two confirmed lensed quasars are presented. Here, μ represents the magnification, while m_{PSF} denotes the magnitude of the multiple images.

name	μ	band	m_{PSF}
J0746+1344 A	2.150	<i>g</i>	20.41 ± 0.13
		<i>r</i>	20.07 ± 0.11
		<i>z</i>	19.99 ± 0.08
J0746+1344 B	-1.610	<i>g</i>	19.26 ± 0.05
		<i>r</i>	18.49 ± 0.01
		<i>z</i>	18.56 ± 0.01
J2121-0826 A	2.868	<i>g</i>	20.01 ± 0.07
		<i>r</i>	19.92 ± 0.07
		<i>z</i>	19.30 ± 0.06
J2121-0826 B	-1.678	<i>g</i>	21.68 ± 0.56
		<i>r</i>	21.50 ± 0.49
		<i>z</i>	21.07 ± 0.45

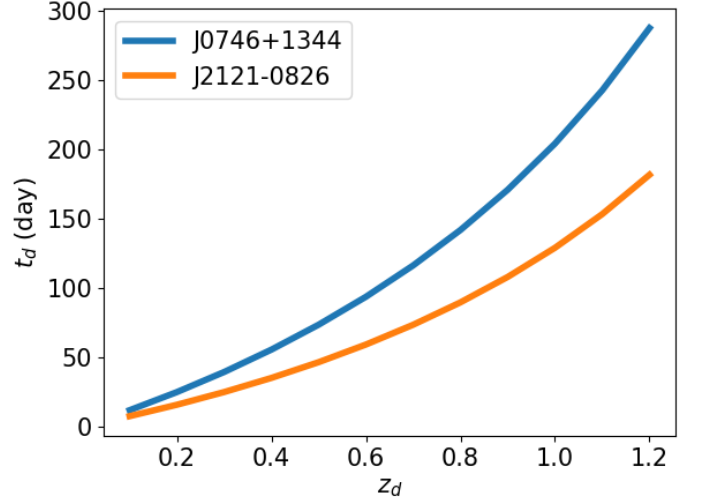


Fig. 5. The time-delay as a function of z_d of two confirmed lensed quasars.

3.1.2. J2121-0826

In Legacy Survey Imaging, the *r*-band magnitudes of two images are 19.63 and 20.55 respectively, which are separated by $1.''34$. Spectroscopic analysis of the DBSP data reveals a blended quasar spectrum at a redshift of $z = 2.395$. The system exhibits two distinct detections in Gaia data, suggesting the presence of multiple images. In the residual of Legacy Survey Imaging, a red component becomes visible after subtracting two PSFs. The *grz*-band composite image is well-modelled by simultaneously fitting a Sérsic profile positioned between the two PSFs, see the bottom line of Figure 3 for this, consistent with the presence of a lensing galaxy. Based on these evidence - the blended high-redshift quasar spectrum, multiple Gaia detections, and the presence of a red component consistent with a lensing galaxy - we classify this system as a gravitational lens.

The Sérsic parameters are presented in Table 2. The PSF parameters can be found in Table 3. The SIE parameters are detailed in Table 4. Additionally, the time delay as a function of lens redshift is shown in Table 5.

3.2. Likely lensed quasars

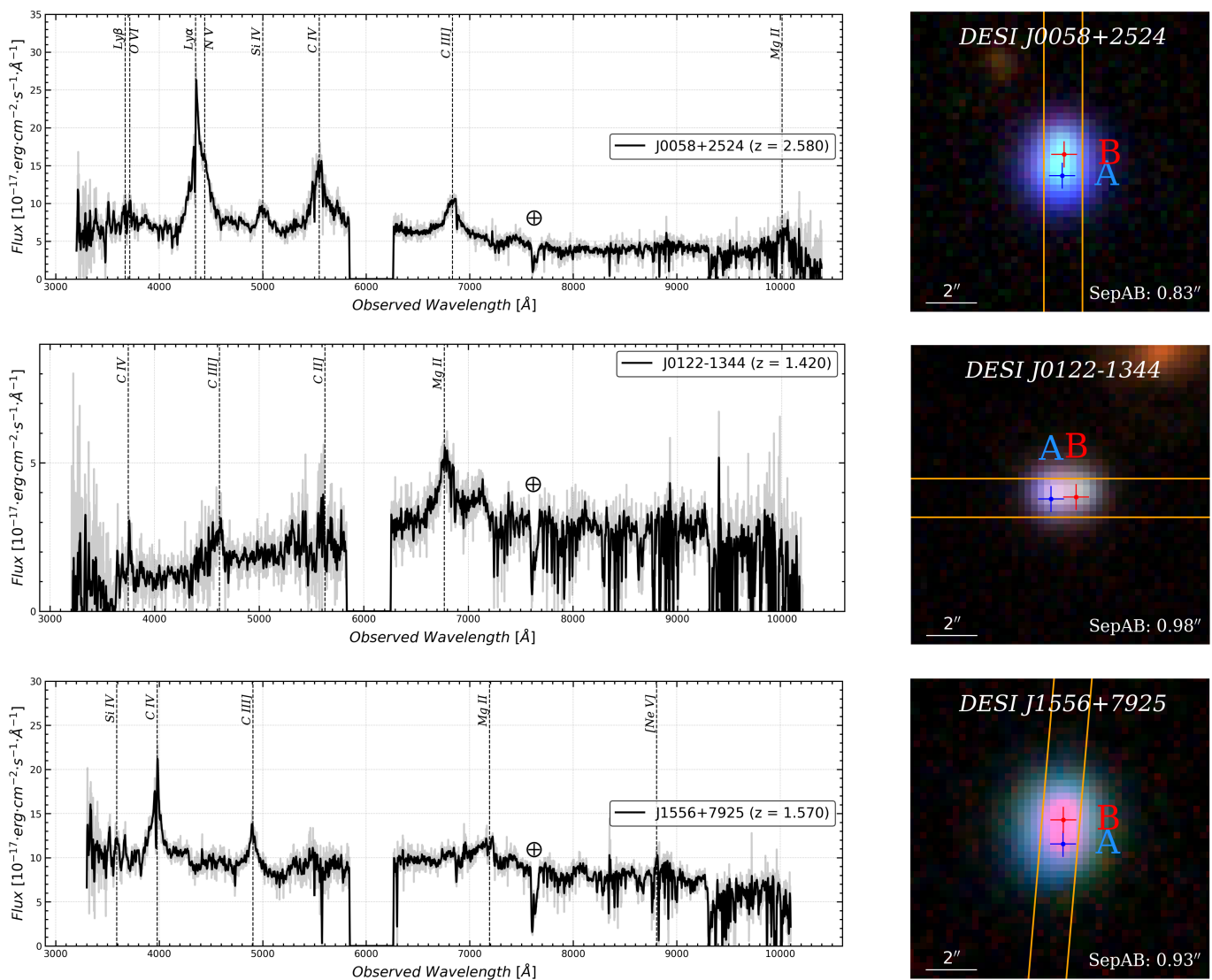
3.2.1. J0058+2524

According to Legacy Survey Imaging, the *r*-band magnitudes of two images are 18.94 and 19.71 respectively; two quasars are separated by $0.''83$. We have exposed this for 1600s. Spectroscopic analysis of the DBSP data reveals a blended quasar spectrum at a redshift of $z = 2.580$, accompanied by two distinct detections in Gaia data. When modelled using a combination of two PSFs and one Sérsic profile, a potential lensing galaxy is detected between the two PSFs, albeit at a low significance level of $\sim 1\sigma$.

The presence of a blended quasar spectrum at $z = 2.58$ and multiple Gaia detections are promising indicators of a gravitational lensing system. However, the low detection significance of the lensing galaxy introduces uncertainty into this classification. Given the ambiguity regarding the lensing galaxy detection, we

Table 4. SIE parameters of two confirmed lensed quasars. The parameters are defined at Appendix A.

name	θ_E (")	q	ϕ (deg)	RA (°)	Dec (°)
J0746+1344	1.208 ± 0.058	0.622 ± 0.102	6.290 ± 3.865	116.649	13.73955
J2121-0826	0.770 ± 0.028	0.839 ± 0.030	-30.353 ± 13.430	320.384723	-8.43616


Fig. 6. The DBSP/P200 spectra and their corresponding cutout images of the three likely lensed quasars. The slit placement is labeled by the yellow lines.

conclude that deeper, higher-resolution imaging is necessary to conclusively confirm or refute this gravitational lens candidate.

3.2.2. J0122-1344

From Legacy Survey Imaging, two point-like components with different colours are visible. In the residual imaging of Legacy Survey Imaging, an extended yellow component is clearly seen. We performed light modelling on this system, and the results are summarised in Table 5. Here are three key observational facts: Firstly, typical quasar broad-line emissions, such as C_{IV} and Mg_{II} , can be identified from the blended spectrum, indicating the presence of at least one quasar. However, the continuum is very different from typical AGN continuum. Secondly, an extended galaxy is clearly visible from Sérsic + two PSF light mod-

elling, with results indicating the Sérsic galaxy with magnitudes of $m_r = 19.48$ and $m_z = 20.51$. Thirdly, Figure 7 presents the $g-r$ vs $r-z$ plot for two images. Both the magnitudes from DESI-LS and our modelling are shown. The results from DESI-LS suggest the image B is more possible a star, image A is more possible a quasars, while our light modelling indicates that both images are quasars.

These observations can be explained by two scenarios.

- Lensing Scenario. Images A and B are doubly-imaged quasars. A bright lensing galaxy significantly contributes to the spectrum, causing the continuum to deviate from a typical quasar spectrum. The color difference between the two images can be attributed to the blended light from the lensing galaxy.

Table 5. Magnitudes of J0122-1344, including both the Sérsic and PSF components, are presented. This includes photometry from this study as well as data from Legacy Survey Imaging. The LS recognised this system as only two PSFs, the Sérsic component is not suitable.

	$g(\text{LS})$	$r(\text{LS})$	$z(\text{LS})$	$g(\text{this work})$	$r(\text{this work})$	$z(\text{this work})$
Sérsic		-		>23	20.51	19.48
J0122A	20.32	19.9	19.37	20.29	20.04	19.78
J0122B	21.04	20.32	19.93	21.08	20.87	20.90

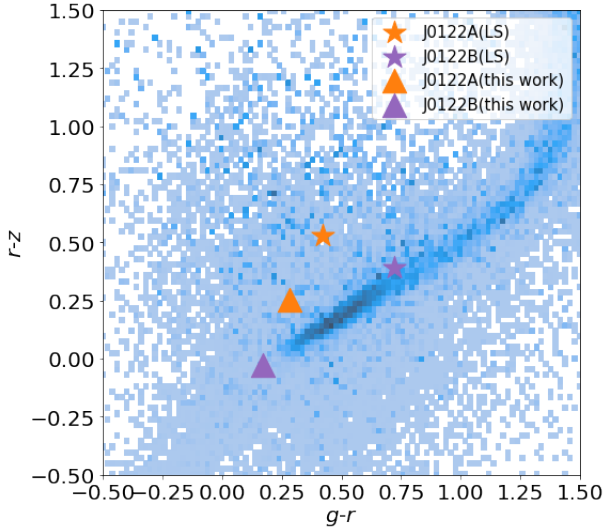


Fig. 7. The colour-colour plot for J0122-1344 is displayed, with blue points indicating stars. The yellow and purple pentagrams represent J0122-1344A based on Legacy Survey Imaging photometry. Furthermore, the yellow and purple triangles correspond to J0122-1344A and J0122-1344B, respectively, as determined by the light modelling results from this study, which utilises two PSFs along with one Sérsic profile (refer to Appendix A).

- Quasar-Galaxy-Star Scenario. The two images represent a quasar-star pair, with a galaxy coincidentally positioned between them. According to Figure 7, the lensing scenario is more plausible because the colour of two images are differ from typical star locations.

To distinguish between these scenarios, improved spectroscopic observations that can capture two distinct spectra from the two point sources are necessary.

3.2.3. J1556+7925

The DBSP data reveals a blended quasar spectrum at $z=1.507$, and two distinct Gaia detections support the hypothesis that this system is a lensed quasar. However, no lensing galaxy is detectable after subtracting two PSFs in the Legacy Survey imaging. We believe deeper imaging is necessary to confirm this candidate.

3.3. Dual quasars

3.3.1. J1759+3459

Spectroscopic analysis reveals the presence of two distinct quasars at redshifts $z = 1.970$ and $z = 1.982$, respectively. The difference in redshifts effectively rules out the possibility of gravitational lensing. We classify this system as a binary quasar pair with an angular separation of $\Delta\theta = 2.3''$, corresponding to a projected physical separation of 19.57 kpc at $z = 1.970$.

The line-of-sight velocity difference between the two quasars is $\Delta v = 1208 \pm 14 \text{ km/s}$.

3.3.2. J1929+6009

Spectroscopic analysis reveals the presence of two distinct quasars at a redshift of $z = 3.277$, separated by an angular distance of $\Delta\theta = 1.34''$. The possibility of gravitational lensing can be confidently ruled out due to the significant differences observed in the continuum spectra of the two quasars. These spectral variations may be attributed to differences in the accretion disk properties, dust extinction, or host galaxy contributions between the two quasars. We classify this system as a dual quasar pair with a projected physical separation of 13.4 kpc at the observed redshift, featuring a velocity difference of less than 10 km/s .

3.4. Projected quasars

3.4.1. J0422+0047

Initially thought to be a gravitationally lensed quasar system with the central yellow component acting as the lensing galaxy, this intriguing configuration has been revealed to be more complex. Spectroscopy of the two quasar objects and the central component has definitively ruled out the lensing scenario due to the significant quasar redshift differences observed.

The large Δv of $11633 \pm 14 \text{ km/s}$ between the quasars leads us to classify this system as a chance alignment of two projected quasars with an intervening galaxy. Despite not being a gravitational lens, this serendipitous alignment enables us to investigate the CGM properties of both the quasar host galaxies and the intervening galaxy.

3.4.2. J2303+0814

Spectroscopic analysis reveals two distinct quasars with significantly different redshifts of $z = 0.948$ and $z = 0.928$, respectively. The substantial difference in their continuum spectra, coupled with the redshift difference, definitively rules out the possibility of gravitational lensing. The redshift difference between the two quasars is $\Delta z = 0.020$, which translates to a line-of-sight velocity difference of $\Delta v = 8583 \pm 22 \text{ km/s}$. This large velocity separation far exceeds what would be expected for physically associated quasars, further supporting our classification.

4. Inspection on available data-sets

We conducted a cross-match between H22 systems and several spectroscopic datasets with radius equals $1''$ (DESI-EDR and SDSS-DR16). Our analysis revealed new dual quasars (Section 4.1) and projected quasars (Section 4.2). To the best of our knowledge, these systems have not been previously discussed in the literature.

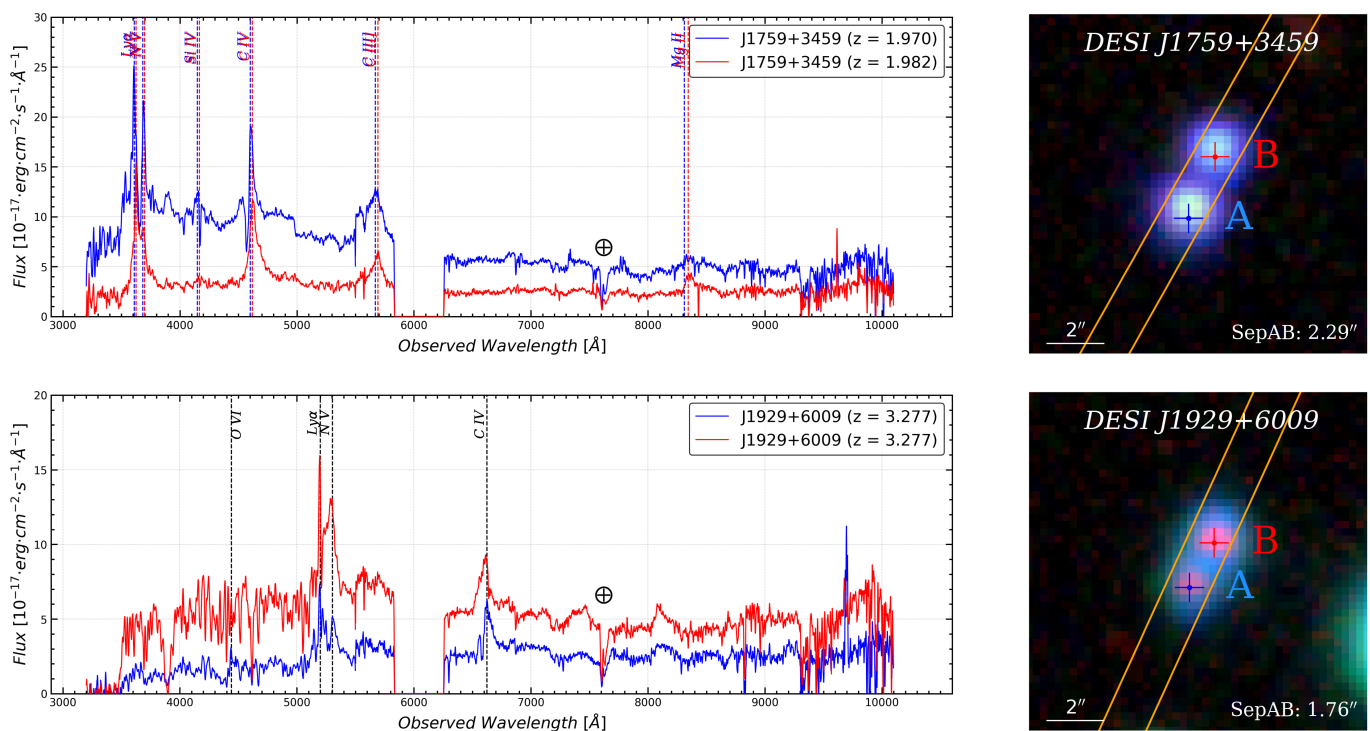


Fig. 8. The DBSP/P200 spectra and their corresponding cutout images of the two dual quasars. The slit placement is labeled by the yellow lines.

Table 6 summarizes the key information for these quasar systems, including their Right Ascension (RA), Declination (Dec), data source, angular separation, redshifts, and associated redshift errors. Figure 10 presents the spectra of the dual quasars, along with their velocity differences (Δv) and projected separations.

4.1. Dual quasars

4.1.1. J0043+0424

Spectroscopic analysis from BOSS reveals that two of the systems exhibit characteristic broad emission lines typical of AGN. Notably, a self-absorption feature is observed in the C_{IV} emission line of quasar A, while it is absent in quasar B. This distinct spectral difference strongly suggests that we are observing a dual quasar system at $z = 2.458$ and $z = 2.445$ separated by $\Delta\theta = 2.78''$ rather than a gravitationally lensed quasar. On the other hand, the small $\Delta v = 1116 \pm 25 \text{ km/s}$ suggest they are not projected quasars. Thus we classify it as dual quasars.

4.1.2. J0154-0048

The spectra from BOSS exhibit typical AGN features, including prominent broad emission lines such as C_{III} , with slightly different redshifts between the two quasars. The redshift difference corresponding to a Δv of $680 \pm 141 \text{ km/s}$. According to studies by Oguri & Marshall (2010) and Cao et al. (2023), the z -band magnitude (m_z) for such lensing systems typically ranges from 14 to 21, which is brighter than the detection limit of the Legacy Imaging Surveys. Given this, we would expect to detect a deflector if this were a gravitational lens system. However, no such deflector is observed. Consequently, we classify this system as a dual quasar with a separation of $\Delta\theta = 2.3''$ or $d = 19.48 \text{ kpc}$ at $z = 1.4817$.

4.1.3. J1424+3439

Spectroscopic analysis from DESI reveals two sources exhibiting quasar characteristics at slightly different redshifts, which can be transferred to a Δv of $87 \pm 39 \text{ km/s}$. Furthermore, no evidence of a gravitational lens deflector is detected in the residual images from the Legacy Survey. Consequently, we classify this system as a dual quasar pair with a projected separation of $\Delta\theta = 2.07''$ or $d = 17.31 \text{ kpc}$ at $z = 1.4716$.

4.1.4. J1643+3156

Spectroscopic analysis from SDSS and BOSS confirms that components A and B are both quasars at approximately $z = 0.586$. According to studies by Oguri & Marshall (2010) and Cao et al. (2023), the m_z of a potential lensing galaxy for a system with $z_s = 0.586$ should be brighter than 17. Such a galaxy would be unambiguously detectable in the Legacy Imaging Surveys. Given the absence of any visible deflector galaxy in the LIS data, we can rule out the lensing scenario for this system. Therefore, we classify this system as a dual quasar pair with a projected separation of $\Delta\theta = 2.33''$ or $d = 15.44 \text{ kpc}$ at $z = 0.5853$. The velocity difference is $67 \pm 12 \text{ km/s}$.

4.2. Projected quasars

4.2.1. J0134+3308

The spectra under examination are from the BOSS. This particular case presents an intriguing projected quasar pair with an angular separation of $3.56''$. While the two quasars exhibit remarkably similar colours, their redshifts differ significantly, with one at $z = 0.7064$ and the other at $z = 1.1359$. Interestingly, both quasars show evidence of their host galaxies in the spectral residuals after subtracting the quasar contribution.

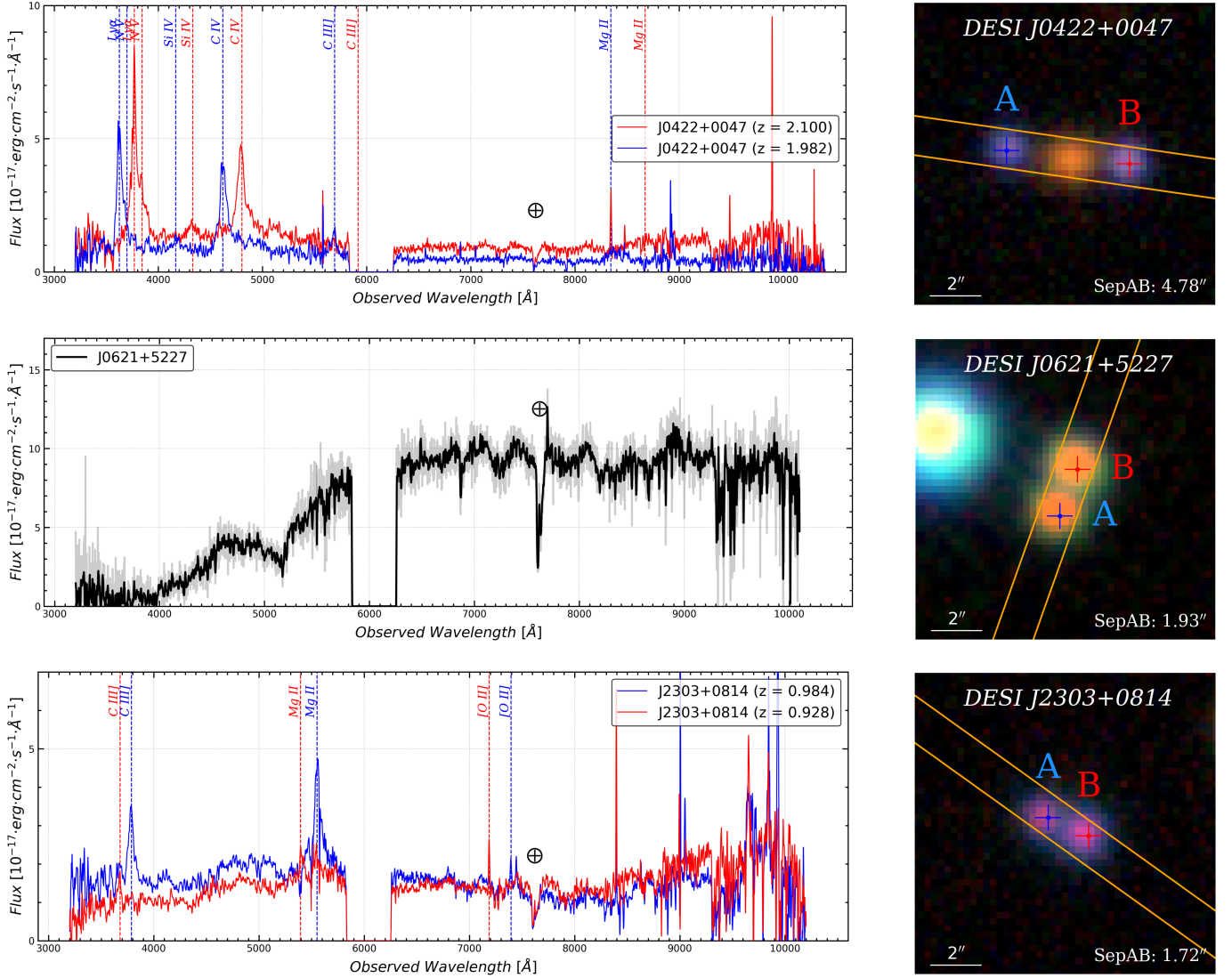


Fig. 9. The DBSP/P200 spectra and their corresponding cutout images of the two projected quasars and one star-star system (J0621+5227). The slit placement is labeled by the yellow lines.

4.2.2. J0843+4733

The broad-line emissions like C_{IV} , C_{III} , Mg_{II} are identified for both quasars. Of particular interest is the spectrum of quasar A, which displays a significant C_{III} absorption feature at $\sim 4000\text{\AA}$. This absorption is potentially due to the presence of quasar B at a lower redshift. Such a configuration presents a valuable opportunity for investigating the CGM of the quasar host galaxy.

4.2.3. J1201-0117

The DESI-EDR spectra reveal two quasars at markedly different redshifts: one at $z = 2.5797$ (quasar A) and another at $z = 1.0653$ (quasar B). A emission of 9400\AA seems not a AGN typical emission, probably from atmosphere.

4.2.4. J1246+5030

The SDSS spectra reveal two quasars at significantly different redshifts: one at $z = 2.7307$ (quasar A) and another at $z = 2.1129$ (quasar B). This substantial redshift difference creates an intriguing

cosmic alignment that offers a unique opportunity for studying quasar absorption systems. In the spectrum of the higher-redshift quasar A, a significant C_{IV} absorption feature is clearly seen. This absorption is particularly interesting as it may be due to the presence of quasar B, which lies at a lower redshift along the same line of sight.

4.2.5. J1351+5224

BOSS spectroscopic observations reveal two quasars with significantly different redshifts ($z = 3.2027$ and $z = 0.9747$). The spectrum of quasar A exhibits a prominent, broad Lyman- α emission line accompanied by the characteristic Lyman- α forest.

4.2.6. J1537+3649

BOSS spectroscopic observations reveal two quasars with distinctly different redshifts ($z = 1.3850$ and $z = 1.0629$). Based on this significant redshift discrepancy, we classify this system as a projected quasar pair separated by $\Delta\theta = 2.53''$.

4.2.7. J1603+5449

DESI-EDR spectroscopic observations reveal two quasars with distinctly different redshifts ($z = 1.5171$ and $z = 0.3451$). Based on this significant redshift discrepancy, we classify this system as a projected quasar pair separated by $\Delta\theta = 2.24''$.

4.2.8. J1655+3408

Spectroscopic analysis from the DESI-EDR confirms that quasars A and B are distinct objects. They are separated by a projected separation of $d = 28.25$ kpc at $z = 1.7316$. The individual redshifts of the quasars ($z = 1.7316$ and $z = 1.6931$ respectively) yield a velocity difference of 4261 ± 37 km/s, which exceeds conventional boundary for dual quasars (2,000 km/s, Hennawi et al. 2010). Consequently, we classify this system as projected quasar pair.

4.2.9. J1758+6654

DESI-EDR spectroscopic data reveals a pair of quasars with markedly different redshifts ($z = 1.9550$ and $z = 2.9151$). The spectrum of the higher-redshift quasar (B) exhibits a significant Mg_{II} absorption feature at $\sim 8400\text{\AA}$. Intriguingly, this absorption may be attributed to the presence of the lower-redshift quasar (A), suggesting the light emitted by quasar B is absorbed by A, despite their considerable redshift difference.

5. Summary and Discussion

In this study, we conducted follow-up spectroscopic observations of lensed-quasar candidates from the previously compiled H22 catalogue (He et al. 2023). These observations took place on October 15-16, 2023, at the Palomar Observatory in California, utilising the P200/DBSP instrument. Additionally, we cross-checked all H22 candidates with publicly available spectroscopic surveys, including DESI-EDR and SDSS. Through the combined efforts of Legacy Survey Imaging, DBSP/P200, and existing spectroscopic surveys, we successfully confirmed two lensed quasars, six dual quasars, and eleven projected quasar pairs.

- Strongly Lensed Quasars: J0746+1344 and J2121-0826 are two lensed quasars at $z_s = 3.105$ and $z_s = 2.395$. Assuming SIE mass model, the θ_E of the lensing system are $1''.208$ and $0''.749$, respectively. Both lenses were confirmed through DBSP spectroscopy.
- Dual Quasars: We identified six dual quasars, with two confirmed by DBSP spectra and the remainder from public datasets. The mean redshift of these pairs is 1.96, with J1929+6009 at $z = 3.28$ being the highest redshift pair and J1643+3156 at $z = 0.59$ the lowest. The projected physical separations range from 15.44 to 22.54 kpc.
- Projected Quasar Pairs: Eleven projected quasar pairs were confirmed, two through DBSP spectra and the rest from public datasets. The projected physical separations of these pairs, ranging from 10.96 to 39.07 kpc, make them suitable for studying the CGM of the lower redshift quasars (Lau et al. 2018; Chen et al. 2023).
- Potential Lensed Quasars: Based on DBSP spectra and Legacy Survey Imaging, we identified three potential lensed quasars. These candidates require deeper imaging or resolved spectra for each image to conclusively determine their lensing nature.

One of the confirmed lensed quasars, J0746+1344, exhibits a strong flux anomaly. The lensing galaxy is located next to the brightest image (image B), which is unusual since the opposite configuration is typically observed. According to Legacy Survey Imaging, over a two-year baseline, the magnitude of image B is more than one magnitude brighter than that of image A in the *grz* bands. This is likely due to an ongoing microlensing effect.

We note that J0746+1344 lies within the WFST wide-file survey footprint (Chen et al. 2023), making it ideal candidate for time delay measurement, provided its time delay is less than 90 days. Both of the confirmed lensed quasars can be monitored by the Muztagh-Ata 1.9-meter Synergy Telescope (MOST, see e.g., Zhu et al. 2023) in the future. Projected quasar pairs serve as exceptional cosmic probes, playing a crucial role in studying the CGM of quasar hosts and their environments. Among our discoveries, J0422+0047 stands out as a particularly intriguing system. It offers the unique opportunity to simultaneously explore the CGM in both the outskirts of the quasar host and a coincidentally overlapped foreground galaxy. This rare configuration provides valuable insights into the diverse environments of the CGM, highlighting differences between AGNs and quiescent elliptical galaxies. For the potential lensed quasars, deeper and higher resolution imaging can be anticipated from future missions such as Euclid (Laureijs et al. 2011; Euclid Collaboration et al. 2024), Chinese Space Station Telescope (CSST; Cao et al. 2018), and Roman (Eifler et al. 2021). If confirmed, although their individual light curves cannot be resolved or separately covered by WFST or MOST, time-delay measurements can still be conducted using blended light curves (Shu et al. 2022).

In addition, we would like to emphasise an intriguing dual quasar discovered by P200, J1929+6009 at $z = 3.28$. The redshift difference between the two components is less than 0.0001, and the projected separation is 19.28 kpc. In Hennawi et al. (2010), 24 dual quasars were identified within a redshift range of 3 to 4, with a mean projected separation of 267 kpc. This highlights the uniqueness of the J1929+6009 system: its projected separation of 19.28 kpc at $z = 3.28$ is notably small. Another interesting aspect is numerous absorptions span the range of 3500 Å to 5200 Å have been observed on the blue side of J1929+6009B, which are not visible in J1929+6009A, although they are only separated by $\Delta\theta = 1.76''$ and at the same redshift. As illustrated in Figure 12, the most prominent feature appears to be a $Ly\beta$ absorption at $z = 2.797$. However, no counterpart can be found a such a redshift in the public available spectra data-sets.

Acknowledgements. This research uses data obtained through the Telescope Access Program (TAP), which has been funded by the TAP association, including Centre for Astronomical Mega-Science CAS(CAMS), XMU, PKU, THU, USTC, NJU, YNU, and SYSU. We thank the anonymous referee for very valuable and constructive comments that help us to improve the paper significantly. We thank Jiao Li, Chao Liu for insightful discussions. We thank *astropy*, *pandas*, *matplotlib*, *astrocrappy*, *lenstronomy* for providing convenient and reliable python packages.

Z.H. acknowledges support from the China Postdoctoral Science Foundation under Grant Number GZC20232990 and the National Natural Science Foundation of China (Grant No. 12403104). R.L. acknowledges the support of the National Nature Science Foundation of China (No 12203050). Y.S. acknowledges the support from the National Science Foundation of China (12333001) and the China Manned Space Program through its Space Application System. G.L. acknowledges the support of the China Manned Spaced Project (CMS-CSST-2021-A12). N.L. acknowledges the support of the CAS Project for Young Scientists in Basic Research (No. YSBR-062), the science research grants from the China Manned Space Project (No. CMS-CSST-2021-A01), and the hospitality of the International Centre of Supernovae (ICESUN), Yunnan Key Laboratory at Yunnan Observatories, Chinese Academy of Sciences. D.D.S. acknowledges the support from the National Science Foundation of China (12303015) and the National Science Foundation of Jiangsu Province (BK20231106).

This project used data obtained with the Dark Energy Camera (DECam), which was constructed by the DES collaboration. Funding for the DES Projects has

Table 6. The information of the confirmed dual quasars (DQ) and projected quasars (PQ) from publicly available data-sets.

Name	H22-ID	RA(°)	Dec(°)	magr	Separation (")	Quasar Redshift (z)	Dataset	outcome
J0043+0424A	2615890	10.970369	4.4076394	20.0954	2.78	2.4581 ± 0.0003	BOSS-DR16	DQ
J0043+0424B		10.969656	4.4073359	21.1319		2.4453 ± 0.0005	BOSS-DR16	
J0154-0048A	11418744	28.709636	-0.80441733	21.4140	2.30	1.4817 ± 0.0004	BOSS-DR16	DQ
J0154-0048B		28.70941	-0.80501563	21.9943		1.4761 ± 0.0011	BOSS-DR16	
J1424+3439A	10410046	216.0092993	34.65426983	21.6626	2.07	2.0117 ± 0.0003	DESI-EDR	DQ
J1424+3439B		216.009599	34.65375044	21.6028		2.0126 ± 0.0002	DESI-EDR	
J1643+3156A	10446316	250.79745	31.939072	19.5198	2.33	0.5863 ± 0.0001	BOSS-DR16	DQ
J1643+3156B		250.79726	31.938444	18.1591		0.5867 ± 0.00003	SDSS-DR16	
J0134+3308A	10428646	23.570643	33.1485	19.1408	3.56	1.1359 ± 0.0006	BOSS-DR16	PQ
J0134+3308B		23.569548	33.148871	19.9502		0.7064 ± 0.0001	BOSS-DR16	
J0843+4733A	10232318	130.74015	47.56241	20.0026	3.42	1.6778 ± 0.0002	BOSS-DR16	PQ
J0843+4733B		130.73904	47.561825	19.4983		1.5549 ± 0.0003	SDSS-DR16	
J1201-0117A	11421719	180.1501026	-1.29273836	20.9270	2.26	2.5797 ± 0.0002	DESI-EDR	PQ
J1201-0117B		180.1494852	-1.29285373	20.7197		1.0653 ± 0.0002	DESI-EDR	
J1246+5030A	2111676	191.55732	50.51334	19.4188	2.61	2.7307 ± 0.0005	BOSS-DR16	PQ
J1246+5030B		191.55674	50.513965	18.3434		2.1129 ± 0.0002	BOSS-DR16	
J1351+5224A	1028812	207.62799	52.401211	19.6030	2.66	3.2027 ± 0.0005	BOSS-DR16	PQ
J1351+5224B		207.62737	52.401845	20.7675		0.9747 ± 0.0002	BOSS-DR16	
J1537+3649A	10343393	234.13051	36.819902	20.7280	2.53	1.3850 ± 0.0005	BOSS-DR16	PQ
J1537+3649B		234.13123	36.819501	21.2257		1.0629 ± 0.0006	BOSS-DR16	
J1603+5449A	10143011	240.8114993	54.81770645	21.5314	2.24	1.5171 ± 0.0003	DESI-EDR	PQ
J1603+5449B		240.8120508	54.81824093	21.9013		0.3451 ± 0.0002	DESI-EDR	
J1655+3408A	10414988	253.7660233	34.13442421	21.2080	3.34	1.7316 ± 0.0001	DESI-EDR	PQ
J1655+3408B		253.7655554	34.13358145	20.2031		1.6931 ± 0.0003	DESI-EDR	
J1758+6654A	10040521	269.4174023	66.90915019	21.4507	2.40	1.9550 ± 0.0002	DESI-EDR	PQ
J1758+6654B		269.4186132	66.90868133	22.2050		2.9151 ± 0.0003	DESI-EDR	

been provided by the U.S. Department of Energy, the U.S. National Science Foundation, the Ministry of Science and Education of Spain, the Science and Technology Facilities Council of the United Kingdom, the Higher Education Funding Council for England, the National Center for Supercomputing Applications at the University of Illinois at Urbana-Champaign, the Kavli Institute of Cosmological Physics at the University of Chicago, Center for Cosmology and Astro-Particle Physics at the Ohio State University, the Mitchell Institute for Fundamental Physics and Astronomy at Texas A&M University, Financiadora de Estudos e Projetos, Fundacao Carlos Chagas Filho de Amparo, Financiadora de Estudos e Projetos, Fundacao Carlos Chagas Filho de Amparo a Pesquisa do Estado do Rio de Janeiro, Conselho Nacional de Desenvolvimento Científico e Tecnológico and the Ministerio da Ciencia, Tecnologia e Inovacao, the Deutsche Forschungsgemeinschaft and the Collaborating Institutions in the Dark Energy Survey. The Collaborating Institutions are Argonne National Laboratory, the University of California at Santa Cruz, the University of Cambridge, Centro de Investigaciones Energeticas, Medioambientales y Tecnologicas-Madrid, the University of Chicago, University College London, the DES-Brazil Consortium, the University of Edinburgh, the Eidgenössische Technische Hochschule (ETH) Zurich, Fermi National Accelerator Laboratory, the University of Illinois at Urbana-Champaign, the Institut de Ciències de l'Espai (IEEC/CSIC), the Institut de Física d'Altes Energies, Lawrence Berkeley National Laboratory, the Ludwig Maximilians Universität München and the associated Excellence Cluster Universe, the University of Michigan, NSF's NOIRLab, the University of Nottingham, the Ohio State University, the University of Pennsylvania, the University of Portsmouth, SLAC National Accelerator Laboratory, Stanford University, the University of Sussex, and Texas A&M University.

References

Anguita, T., Schmidt, R. W., Turner, E. L., et al. 2008, *A&A*, 480, 327
Astropy Collaboration, Price-Whelan, A. M., Lim, P. L., et al. 2022, *ApJ*, 935, 167
Blanton, M. R., Bershad, M. A., Abolfathi, B., et al. 2017, *AJ*, 154, 28
Bolton, A. S., Brownstein, J. R., Kochanek, C. S., et al. 2012, *ApJ*, 757, 82
Boylan-Kolchin, M., Ma, C.-P., & Quataert, E. 2008, *MNRAS*, 383, 93
Braibant, L., Hutsemekers, D., Sluse, D., Anguita, T., & García-Vergara, C. J. 2014, *A&A*, 565, L11
Cai, Z., Cantalupo, S., Prochaska, J. X., et al. 2019, *ApJS*, 245, 23
Cao, X., Li, R., Li, N., et al. 2023, arXiv e-prints, arXiv:2312.06239
Cao, Y., Gong, Y., Meng, X.-M., et al. 2018, *MNRAS*, 480, 2178
Chambers, K. C., Magnier, E. A., Metcalfe, N., et al. 2016, arXiv e-prints, arXiv:1612.05560
Chen, Z.-F., Qin, H.-C., Cai, J.-T., et al. 2023, *ApJS*, 265, 46
Dawes, C., Storfer, C., Huang, X., et al. 2023, *ApJS*, 269, 61
de Jong, R. S., Agertz, O., Berbel, A. A., et al. 2019, *The Messenger*, 175, 3

De Rosa, A., Vignali, C., Bogdanović, T., et al. 2019, *New A Rev.*, 86, 101525
DESI Collaboration, Aghamousa, A., Aguilar, J., et al. 2016, arXiv e-prints, arXiv:1611.00036
Dey, A., Schlegel, D. J., Lang, D., et al. 2019, *AJ*, 157, 168
Dux, F., Lemon, C., Courbin, F., et al. 2024, *A&A*, 682, A47
Dux, F., Lemon, C., Courbin, F., et al. 2023, *A&A*, 679, L4
Eifler, T., Miyatake, H., Krause, E., et al. 2021, *MNRAS*, 507, 1746
Euclid Collaboration, Mellier, Y., Abdurro'uf, et al. 2024, arXiv e-prints, arXiv:2405.13491
Fian, C., Mediavilla, E., Motta, V., et al. 2021, *A&A*, 653, A109
Filipp, A., Shu, Y., Pakmor, R., Suyu, S. H., & Huang, X. 2023, *A&A*, 677, A113
Findlay, J. R., Prochaska, J. X., Hennawi, J. F., et al. 2018, *ApJS*, 236, 44
Gaia Collaboration, Brown, A. G. A., Vallenari, A., et al. 2018, *A&A*, 616, A1
Guerras, E., Mediavilla, E., Jimenez-Vicente, J., et al. 2013, *The Astrophysical Journal*, 778, 123
Harris, C. R., Millman, K. J., van der Walt, S. J., et al. 2020, *Nature*, 585, 357
He, Z., & Li, N. 2022, *RAA*, 22, 095021
He, Z., Li, N., Cao, X., et al. 2023, *A&A*, 672, A123
Hennawi, J. F., Myers, A. D., Shen, Y., et al. 2010, *ApJ*, 719, 1672
Hutsemekers, D. & Sluse, D. 2021, *A&A*, 654, A155
Kormann, R., Schneider, P., & Bartelmann, M. 1994, *A&A*, 284, 285
Lau, M. W., Prochaska, J. X., & Hennawi, J. F. 2018, *ApJ*, 857, 126
Laureijs, R., Amiaux, J., Arduini, S., et al. 2011, arXiv e-prints, arXiv:1110.3193
Lemon, C., Anguita, T., Auger-Williams, M. W., et al. 2022, *MNRAS*
Li, R., Napolitano, N. R., Spiniello, C., et al. 2021, *ApJ*, 923, 16
Liao, K., Shafieloo, A., Keeley, R. E., & Linder, E. V. 2019, *ApJ*, 886, L23
Marshall, P. J., Verma, A., More, A., et al. 2016, *MNRAS*, 455, 1171
Martin, G., Kaviraj, S., Devriendt, J. E. G., Dubois, Y., & Pichon, C. 2018, *MNRAS*, 480, 2266
McCully, C., Crawford, S., Kovacs, G., et al. 2018, *astropy/astroscrappy: v1.0.5 Zenodo Release*
Motta, V., Mediavilla, E., Falco, E., & Muñoz, J. A. 2012, *ApJ*, 755, 82
Oguri, M. & Marshall, P. J. 2010, *MNRAS*, 405, 2579
Oguri, M., Rusu, C. E., & Falco, E. E. 2014, *MNRAS*, 439, 2494
Oke, J. B. & Gunn, J. E. 1982, *PASP*, 94, 586
Roedig, C., Krolík, J. H., & Miller, M. C. 2014, *ApJ*, 785, 115
Romero, G. E., Vila, G. S., & Pérez, D. 2016, *A&A*, 588, A125
Shajib, A. J., Treu, T., & Agnello, A. 2018, *MNRAS*, 473, 210
Shu, Y., Bolton, A. S., Brownstein, J. R., et al. 2015, *ApJ*, 803, 71
Shu, Y., Cañameras, R., Schuldt, S., et al. 2022, *A&A*, 662, A4
Sluse, D., Schmidt, R., Courbin, F., et al. 2011, *A&A*, 528, A100
Sonnenfeld, A. & Cautun, M. 2021, *A&A*, 651, A18
Sonnenfeld, A., Treu, T., Gavazzi, R., et al. 2013, *ApJ*, 777, 98
Suyu, S. H., Treu, T., Hilbert, S., et al. 2014, *ApJ*, 788, L35
The Dark Energy Survey Collaboration. 2005, arXiv e-prints, astro
Wes McKinney. 2010, in *Proceedings of the 9th Python in Science Conference*, ed. Stéfan van der Walt & Jarrod Millman, 56 – 61
Wong, K. C., Suyu, S. H., Chen, G. C. F., et al. 2020, *MNRAS*, 498, 1420
Zhu, S., Shu, Y., Yuan, H., et al. 2023, *Research in Astronomy and Astrophysics*, 23, 035001

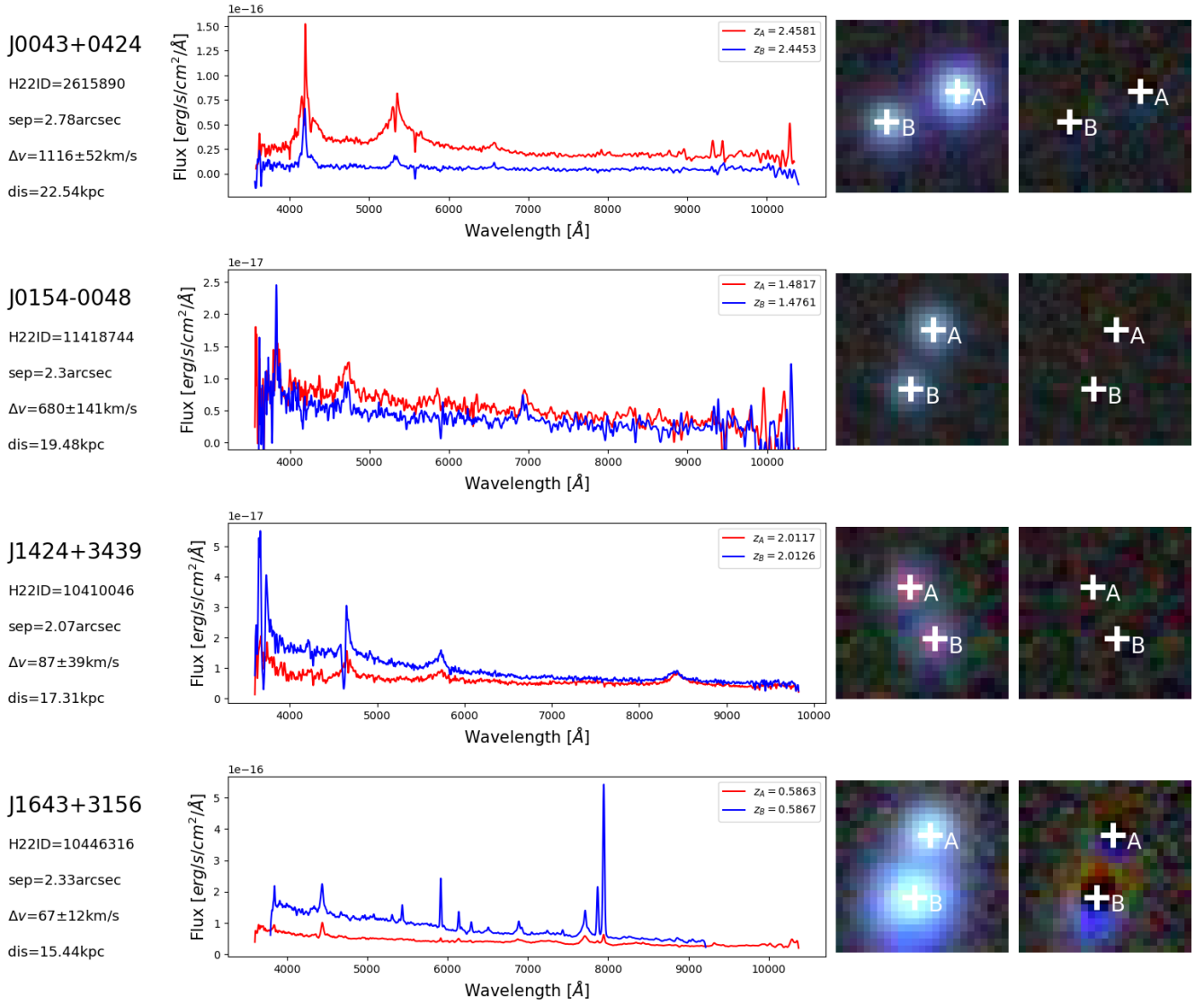


Fig. 10. We present data on four dual quasars, verified using publicly available spectral datasets. On the left, we provide essential details: Δv represents the velocity difference, ‘sep’ denotes the image separation of the two quasars, and ‘dis’ indicates the projected separation in the line-of-sight direction at lower redshift. The second column displays the spectra, where the fluxes have been smoothed using a Gaussian kernel with a standard deviation of 5 \AA . The third column features the *grz* color image from the DESI-LS DR10, while the final column shows the residual image derived from DESI-LS DR10.

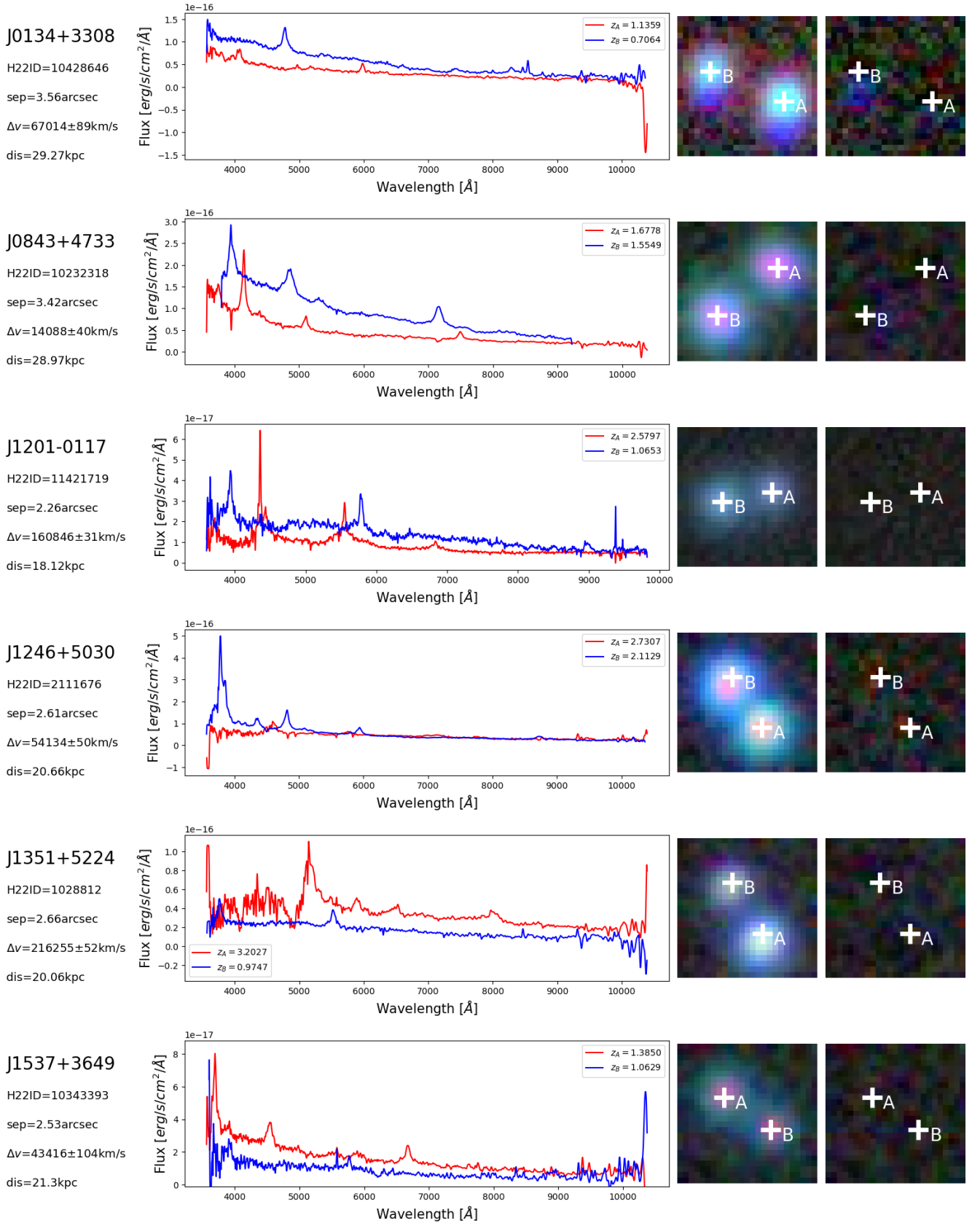


Fig. 11. We present data on nine projected quasars, verified using publicly available spectral datasets. The configuration of this plot is the same with Figure 10.

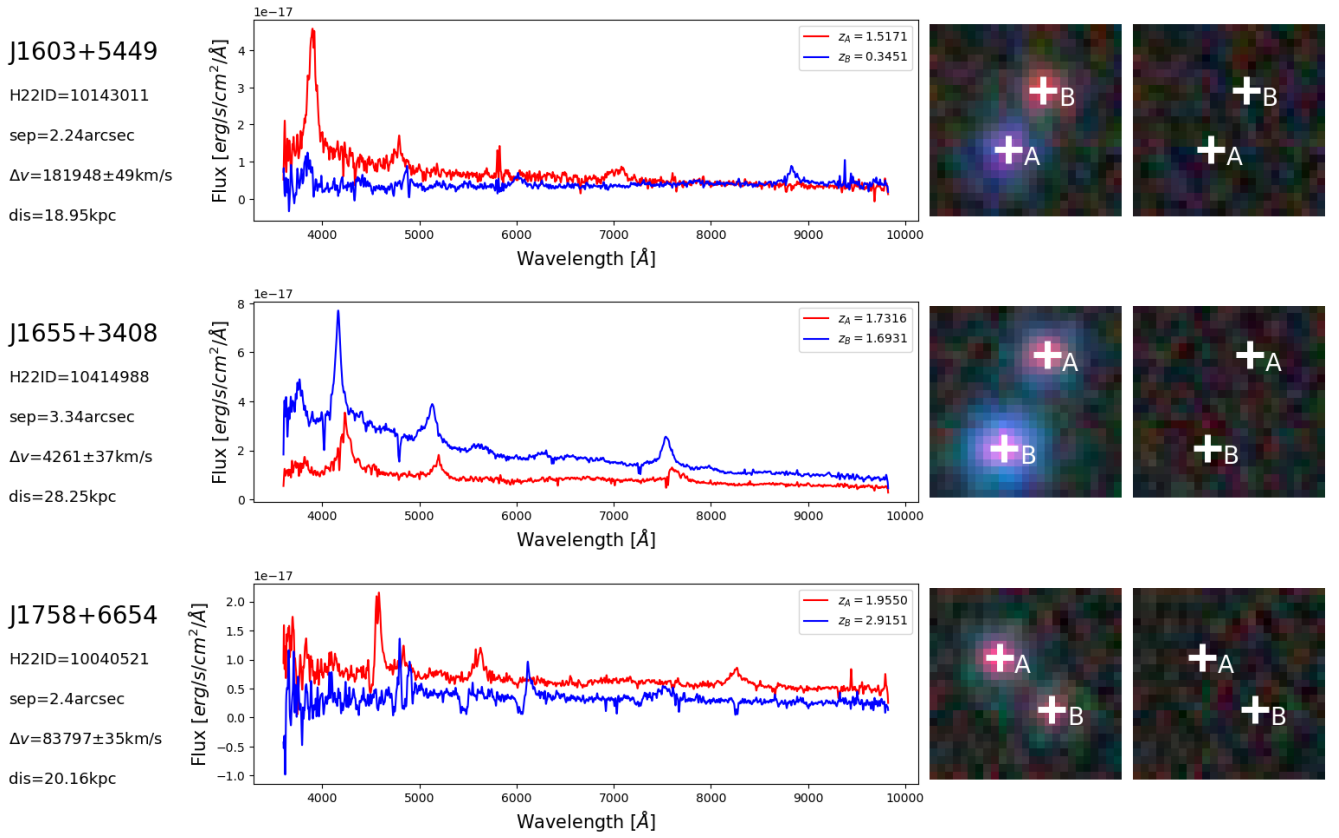


Fig. 11. –Continued.

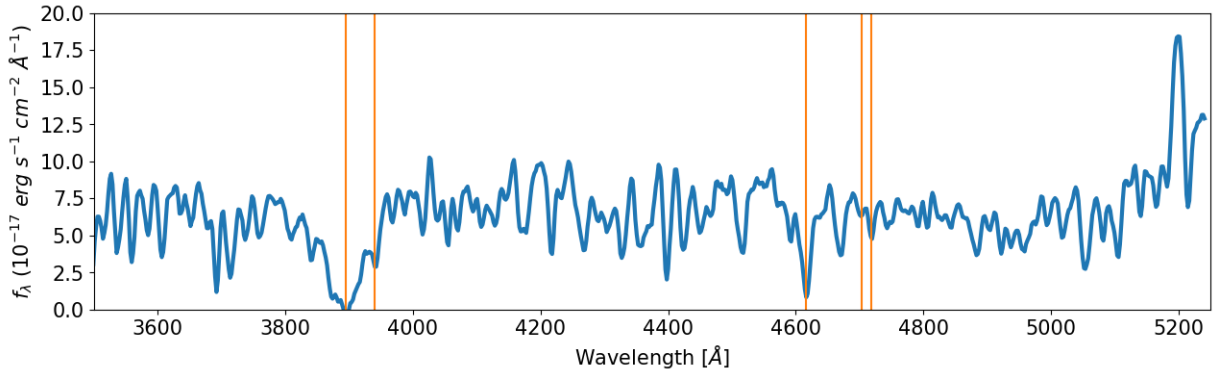


Fig. 12. The blue side spectrum of J1929+6009B spans from 3500Å to 5250Å. The solid orange line represents the absorptions at $z = 2.797$. From left to right, the features are Ly_β , O_{VI} , Ly_α , and N_V doublet.

Appendix A: Light and mass modelling

We use the two-Moffat profile $I_{P,i}$ (i presents the i -th image) to describe the light distributions of the quasars in each band, which can be considered as PSFs in DESI-LS images. $I_{P,i}$ is characterized by the following parameters: the width parameters (α_1, α_2), shape parameters (β_1, β_2), position angles ($\phi_{m,1}, \phi_{m,2}$), offsets between the centres of the first and second Moffat profiles ($\delta x_m, \delta y_m$), the amplitude ratio between the first and second Moffat profiles (f), the amplitude of the first Moffat profile (A_m^i), and the coordinates of the centre of the first Moffat profile (x_m^i, y_m^i). We determine the parameters $\alpha_1, \alpha_2, \beta_1, \beta_2, \phi_{m,1}, \phi_{m,2}, \delta x_m, \delta y_m$, and f through star fitting using a nearby star close to the system of interest, and leaving A_m^i, x_m^i , and y_m^i to be fitted in later procedures. We employ a single Sérsic profile along with i PSFs to model the light distribution of lensed quasar systems. The model can be expressed as:

The Sérsic profile (I_s) is characterized by seven parameters: Sérsic index (n_s), half-light radius (r_s), position angle (ϕ_s), axis-ratio (q_s), amplitude (A_s) and the coordinates of the lens centre (x_{lens}, y_{lens}). Initially, we fit the band exhibiting the most prominent lensing galaxy signal (as indicated by the residual image of Legacy Survey Imaging) to minimise A_m^i, x_m^i , and y_m^i of the PSF model and x_{lens}, y_{lens} of Sersic model use the following likelihood function.

$$\log p(I_{data}|I_{model}) = \frac{(I_{data} - I_{model})^2}{2\sigma_{bkg}^2}, \quad (\text{A.2})$$

where σ_{bkg} denotes the background noise. Subsequently, we fit the other bands using the same procedure. In those fittings, we fix x_m^i, y_m^i, x_{lens} , and y_{lens} according to the results obtained from the first band. The other parameters ($A_m^i, n_s, r_s, \phi_s, q_s$, and A_s) were allowed to be differed among each bands. We adopt a SIE as our lens mass model since it has been shown to align well with observations across numerous studies (see e.g. Bolton et al. 2012; Sonnenfeld et al. 2013). During the lens modelling process, we assume that the SIE halo shares the same centre as the Sérsic profile previously determined (x_{lens}, y_{lens}). Here, to avoid the effect of microlensing and AGN light-variation, we only fit the positions of multiple images, which are established during the light modelling phase. The parameters adjusted in mass modelling include: Einstein radius (θ_E), axis ratio and position angle of SIE (q_{SIE}, ϕ_{SIE}), and source position (x_{src}, y_{src}). Note that q_{SIE} and ϕ_{SIE} were constrained within a range centered on q_s and ϕ_s , which were determined during the light modeling stage based on the results from the band with the highest signal-to-noise ratio for the lensing galaxy. To be specific, q_{SIE} was allowed for a $\pm 30\%$ variation compared to q_s , while ϕ_{SIE} was allowed for a $\pm 30^\circ$ variation compared to ϕ_s . Totally, we used four inputted parameters ($x_m^1, x_m^2, y_m^1, y_m^2$) to constrain five parameters ($\theta_E, x_{src}, y_{src}, q_{SIE}$, and ϕ_{SIE}), and gave q_{SIE} and ϕ_{SIE} priors. The likelihood function used in SIE fitting is that:

$$\log p(\mathbf{r}_i|\mathbf{r}_i^p) = \sum_i \frac{|\mathbf{r}_i - \mathbf{r}_i^p|^2}{\sigma_{p,i}^2} \quad (\text{A.3})$$

with

$$\mathbf{r}_i = \begin{pmatrix} x_m^i \\ y_m^i \end{pmatrix} \quad (\text{A.4})$$

where $\sigma_{p,i}$ represents the astrometric error of i -th image, \mathbf{r}_i^p is the position of multiple images predicted by SIE model. After obtaining all parameters, we can further estimate the time delay by varying the range of z_d , set between 0.1 and 1.25 to encompass the z_d of the majority known lensed quasars. The time delay is defined as:

$$t_d = \text{arrival_time}(\text{Img}_B) - \text{arrival_time}(\text{Img}_A), \quad (\text{A.5})$$

where labels A and B correspond to those in Figure 4. In Figure 5, we illustrate the time delay versus different values of z_d .

$$I_{model} = I_s + \sum_{i=1}^{nimg} I_{P,i} \quad (\text{A.1})$$